Composites: Part A 105 (2018) 291–299

Contents lists available at ScienceDirect

Composites: Part A

journal homepage: www.elsevier.com/locate/compositesa

Highly sensitive and stretchable piezoresistive strain sensor based on conductive poly(styrene-butadiene-styrene)/few layer graphene composite fiber

Xingping Wang [a], Si Meng [a], Mike Tebyetekerwa [a], Yilong Li [b], Jürgen Pionteck [b], Bin Sun [a], Zongyi Qin [a], Meifang Zhu [a,*]

[a] State Key Laboratory for Modification of Chemical Fibers and Polymer Materials, College of Material Science and Engineering, Donghua University, Shanghai 201620, PR China
[b] Leibniz Institute of Polymer Research Dresden, Hohe Straße 6, 01069 Dresden, Germany

ARTICLE INFO

Article history:
Received 12 August 2017
Received in revised form 15 November 2017
Accepted 29 November 2017
Available online 5 December 2017

Keywords:
A: Graphene
A: Polymer-matrix composites (PMCs)
A: Fibers
B: Electrical properties

ABSTRACT

High stretchability and sensitivity are the major desired requirements of strain sensors for wearable electronics applications, especially in health and medical monitoring. Herein, a highly sensitive and stretchable strain sensor based on conductive poly(styrene-butadienestyrene)/few layer graphene (SBS/FLG) composite fiber is fabricated through an easy and scalable wet-spinning process. Owing to the super flexibility of SBS matrix and the excellent electrical and mechanical properties of FLG, the SBS/FLG fiber based strain sensor revealed superior performance, including wide workable strain range (>110%), superior sensitivity (gauge factor of 160 at a strain of 50% and of 2546 at a strain of 100%), and durability. Furthermore, the mechanism behind the excellent performances of SBS/FLG fiber based sensors is discussed in detail.

1. Introduction

The next generation electronics are predicted to be fiber-based with flexible, stretchable, and wearable features. Strain sensors, as an important subpart of wearable electronics, present widespread potential applications including human-motion detection, personalized health monitoring, and human-machine interaction [1,2]. Flexible strain sensor devices are designed to be attached to the clothing or even directly mounted on the human skin to measure the strain induced by human movements. Strain sensors can transduce the mechanical deformations into electrical signals upon stretching and releasing owing to the piezoresistive effect. Effective wearable strain sensors for human motion monitoring must possess high stretchability ($\varepsilon > 50\%$ where ε is the strain), sensitivity, flexibility, stability, and lightweight. Apparently, conventional strain sensors based on semiconducting and metallic materials cannot fulfill the requirements of wearable strain sensors due to their friability and poor stretchability (usually $\varepsilon < 5\%$). To date, various approaches have been proposed to fabricate strain sensors with high stretchability by combining electrical conductive nanomaterials with flexible and stretchable polymers. However, most of the reported strain sensors failed to simultaneously attain high sensitivity (indicated by gauge factor, GF) and high stretchability (indicated by tolerable strain), which limits their applications in monitoring large motions (e.g. joints movements) of the human body. For example, Wang et al. developed a graphene-based strain sensor, which possessed an extremely high GF (1000 under 2–6% strains), but the strain sensor was only able to withstand strains of up to 7% [3]. On the contrary, Yamada et al. reported a highly stretchable carbon nanotubes-polydimethylsiloxane (PDMS) film based strain sensor with wide workable strain range (up to 280%), but the strain sensor only had a GF of 0.06 within a strain range of 200% strain [1]. Lipomi et al. reported a strain sensor based on transparent elastic films of carbon nanotubes that could stretch out to 150% strain. Unfortunately, it exhibited a GF less than 2.6 at 150% strain [4]. Yan et al. reported a highly stretchable graphene-nanocellulose nanopaper that could stretch out to 100% strain, but the GF of the strain sensor was still less than 7.1 [5]. Very recently, Park et al. reported a highly flexible wrinkled carbon nanotube thin film strain sensor which could be stretched to 700%. However, it exhibited a GF of only 0.65 in the strain range of 0–400%, limiting its applications in monitoring most deformations of a human body [6]. Moreover, the fabrication procedures of these strain sensors are complicated and unfit for large-scale production. Thus, it is necessary to develop a facile approach to fabricate polymer based strain sensors with high sensitivity and stretchability.

* Corresponding author.
E-mail address: zhumf@dhu.edu.cn (M. Zhu).

https://doi.org/10.1016/j.compositesa.2017.11.027
1359-835X/

In addition to high sensitivity and stretchability, the stability of the strain sensor is another essential factor as strain sensing applications often require stable electrical resistivity-strain behavior under long time cyclic strains. Instability is usually caused by the poor interaction between conductive nanomaterial fillers and the polymer matrix. For instance, Amjadi et al. reported highly flexible, stretchable sensitive strain sensors based on silver nanowires with PDMS that had a GF of 14 at 70% strain [7]. However, the PDMS based strain sensor exhibited poor stability due to the poor adhesion between the nanowires and PDMS. It was concluded that strong interfacial interaction between conductive fillers and polymer matrix would give better sensing performances [2]. Therefore, in order to fabricate high-performance strain sensor, the polymer substrates should have strong interfacial adhesion with the conductive fillers in addition to high stretchability and excellent processability.

Nanomaterials such as carbon materials (carbon black [8–10], carbon nanotubes [11–13], and graphene [14,15]), metal nanowires [16], and electrically conductive polymers are the most commonly used conductive fillers. Especially, graphene, a two-dimensional hexagonally structured material, consisting of sp^2-bonded carbon atoms, has been considered as a potential candidate for piezoresistive sensors owing to its extraordinary electrical and mechanical properties [17,18]. As polymer matrix, silicone-based elastomers (e.g., PDMS and Ecoflex) and rubbers (e.g., natural rubber and thermoplastic elastomers) have been widely studied. Among these, triblock copolymer poly(styrene-butadienestyrene) (SBS) has been used extensively for strain sensors due to its high stretchability, excellent elastic recovery, and good processability [19–21]. Furthermore, there is a strong interfacial interaction between graphene and SBS owing to the effective π–π interactions between the phenyl groups of SBS and graphene [22]. According to the above discussion, strain sensors based on SBS/FLG composite can be expected to attain high sensitivity and high stretchability simultaneously.

In this work, conductive SBS/FLG fibers (SGFs) were fabricated via a facile and scalable wet-spinning method and evaluated as piezoresistive strain sensors. The influence of FLG contents, applied strain and strain rate on the strain sensing behaviors were investigated by both uniaxial tensile and cyclic stretching-releasing tests. In particular, a modeling approach was used to further investigate the tunneling behavior of these SGFs under strain. Moreover, a schematic illustration of the conductive network evolution under stretching-releasing process was drawn for a better understanding of the strain sensing mechanism.

2. Experimental methods

2.1. Materials and reagents

1 to 5 layers graphene (G-100) was purchased from Shanghai Simbatt Energy Technology Co. Ltd, China. The total oxygen content was 7.0–7.5 wt%, and the conductivity was about 700–1500 S/m. The wrinkled and crumpled structure of graphene was observed (Fig. S1, Supporting information). SBS D1102K triblock copolymer with a butadiene/styrene weight ratio of 72/28 and a density of 0.94 g cm^{-3} was purchased from Kraton, USA. Tetrahydrofuran was purchased from Sinopharm Chemical Reagent Co. Ltd., China. All reagents were of analytical grade and used as received without further purification.

2.2. Spinning solution preparation and fiber spinning

The required amount of FLG was dispersed in 20 mL tetrahydrofuran (THF) and sonicated for 4 h at an output power of 45 W using a digital ultrasonic processor (S-450D-1/2, Branson) in water bath at 20 °C. Then, 3 g SBS was added to the FLG/THF suspension. The solution was agitated at room temperature for 24 h and finally sonicated for another 1 h. The SGFs fibers were fabricated through a facile and scalable wet-spinning process [23,24]. Briefly, the spinning solutions were injected into a rotating ethanol coagulation bath using a 10-mL syringe with a 23-gauge hollow needle (as spinneret). The resulting fibers, which are asymmetrically shaped with a dimension of ca. 60 times 250 μm (see insets in Fig. 1a–c), were drawn out vertically and wound onto a spool.

In this paper, samples are denoted SBS/xG for simplification, where x represents the content of FLG in weight percentage. For instance, SBS/3G represents the composite fiber containing 3 wt% FLG.

2.3. Morphological, mechanical and electrical characterization

The surface and cross-sectional (fractured in liquid nitrogen) morphology of fibers were characterized using a field emission scanning electron microscope JEOL JSM-4800LV. All the samples were sputter coated with platinum. Wide-angle X-ray diffraction (XRD) patterns were taken with 40 kV, 450 mA Cu Kα (the X-ray wave length is 1.54178A) radiation using DMAX/2550PC (Rigaku Denki Instrument). The detector moved step by step ($\Delta 2\theta = 0.02°$) in a scanning range from $2\theta = 5°$ to 60° at a speed of 6° min^{-1}.

Fiber conductivity was measured using the two-point probe method, in which probes were connected to a Keithley 6487 source meter. The electrical conductivity of the fiber was calculated using $\sigma = L/(R \times S)$, where σ (S/cm) is the electrical conductivity, R (Ω) is the electrical resistance, and L (cm) and A (cm^2) are the length and cross section area of the composite fiber, respectively.

The mechanical properties of the fibers were measured using a universal testing machine (Instron 5996). For tensile tests, samples were prepared by attaching the fibers to paper frames (10 mm in aperture), and fibers were stretched to failure at a strain rate of 20 mm min^{-1} (200% min^{-1}). Electromechanical tests were conducted by coupling a digital multimeter (Keithley 6487) to measure the electrical resistance of SGFs during cyclic straining. The sample preparation was similar to the mechanical property test. Copper tapes were attached tightly onto both ends of three fibers to allow for resistance measurements. Silver paste was used to ensure good contact between the copper tape and the fiber. The cyclic stretching-releasing test was performed to investigate the dynamic strain sensing behavior. Samples with a resistance above 1×10^{10} Ω are considered as nonconductive due to the limitation of experimental set-up. All these experiments were carried out at room temperature. The free length of the fibers was set to be 10 mm and the strain rate was 5 mm min^{-1} corresponding to 50% min^{-1}, if not mentioned otherwise.

3. Results and discussion

3.1. Morphology and structure of SGFs

SBS/FLG composite fibers (SGFs) were fabricated using a facile wet-spinning process. The fabrication schematic and photographs of obtained SGFs with different FLG loadings are shown in Fig. S2, Supporting Information. As mentioned earlier, the dispersion of the filler and interfacial interactions are critical to the sensing properties of the composites. To further investigate the FLG dispersion on the electrical and morphological properties of SGFs, the SEM micrographs of SGFs with different FLG loadings are shown in Fig. 1. It can be seen that the fracture surface of the SGFs appears porous, and the porosity increased with increasing FLG

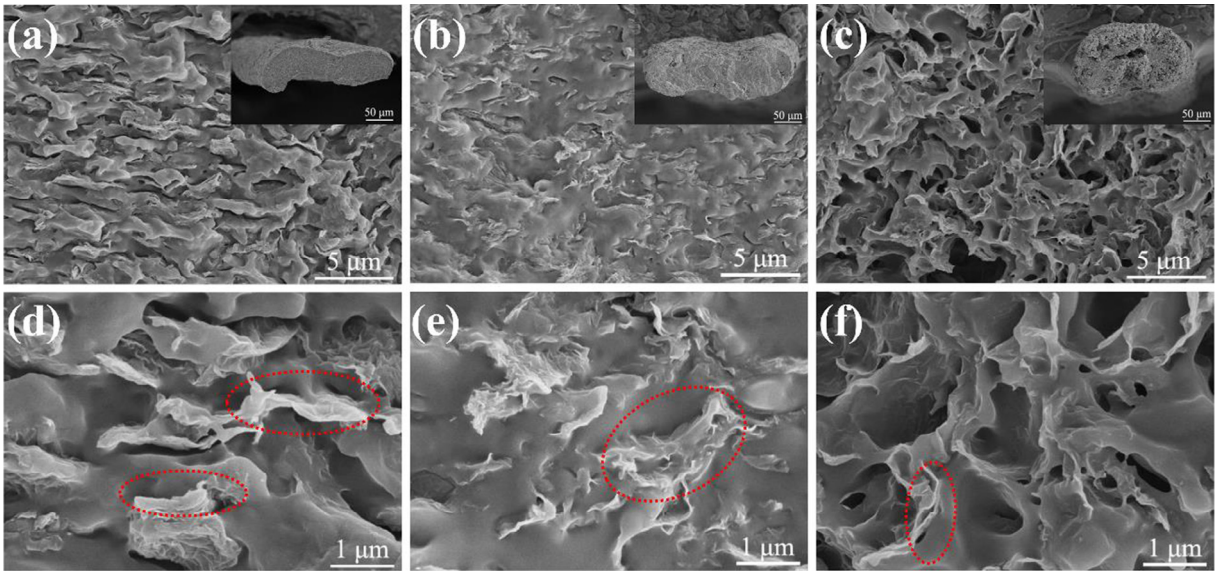

Fig. 1. SEM images of SBS/FLG fibers with FLG loadings of (a) 3 wt%, (b) 5 wt%, (c) 7 wt%, (d), (e), and (f) are higher magnification of (a), (b), and (c), respectively. The inserts are the corresponding cross-section SEM images of SGFs. (For interpretation of the references to colour in this figure legend, the reader is referred to the web version of this article.)

contents (Fig. 1). Moreover, their cross-sectional profiles changed from an irregularly shaped to a more circularly shaped with the increase of FLG loading (insets in Fig. 1a–c). In wet-spinning process, fibers tend to form irregular (or circular) cross-sections when the diffusion rate of the coagulating solvent into the injected spinning solution is higher (or lower) than the extraction rate of the solvent of spinning solution into the coagulation bath, a process normally referred to as the mass transfer rate difference [25]. In this study, it was observed that the morphological changes occurred due to the differences in the coagulation rates arising from the various FLG content. This means the addition of FLG in spinning solution influences the mass transfer rate differences. With the increase of FLG content, it is difficult to achieve good dispersion and the FLG tends to agglomerate to form clusters. As a result, the clusters can form a great quantity of micro-channels which can significantly improve the extraction rate of the solvent of spinning solution into the coagulation bath and suborbicular cross-sections were obtained. Ultimately, the micro-channels develop into microporous during rapid fiber formation/solidification process and hence the porosity increased with increasing FLG contents.

As shown in Fig. 1a, 1b, and 1c, few layer graphene sheets are loosely agglomerated and homogeneously dispersed throughout the SBS matrix without extraction, and the interface between the FLG and SBS is very blurry (see dotted circle in Fig. 1d, 1e, and 1f). All of these observations indicated strong graphene-SBS interfacial interactions. This can be attributed to two major aspects. First, the phenyl groups of graphene are capable of forming π-π stacking with the phenyl groups of SBS [26,27]. Second, the wrinkled surface of FLG can cause an enhanced mechanical interlocking with the SBS chains, leading to better adhesion [28].

The dispersion of FLG in SBS was further characterized by XRD. Fig. S3 (Supporting Information) displays the XRD patterns of FLG and SBS and SBS/FLG composites with different FLG loadings. The diffraction pattern of FLG shows a broad peak with a maximum at $2\theta = 23.7°$ that corresponds to an interlayer spacing of 3.75 Å. This is somehow larger than the interlayer spacing in pure graphite (3.35 Å), certainly caused by some defects in the few layer graphite and the broadness results from its small size. Pure SBS shows a diffuse-like peak ranging from 15° to 26° and centered at 19°, indicating the amorphous nature of SBS [29]. The SBS/FLG composites with different FLG loadings only show one broad peak corresponding to the diffraction of SBS matrix and the FLG is detectable only as soft broadening of the SBS diffraction pattern at the right hand side. It is generally believed that the XRD pattern would cause a diffraction peak at 23.7° if the graphene layers are restacked to larger graphitic structures during the preparation [14]. However, in this work, the disappearance of this separate peak reveals that FLG has been well dispersed in the SBS matrix.

3.2. Electrical properties

The electrical conductivity as a function of FLG loading for the composite fibers is shown in Fig. 2. A drastic conductivity increase of SGFs can be observed when the FLG loading in the range of 2.0–3.0 wt%, which is referred to as the electrical percolation of composites. After percolating, the conductivity increased gently with FLG loading. The relationship between FLG content and electrical conductivity of SGFs was further investigated by the classical statistical percolation theory (Eq. (1)) [30]. Usually, experimental results are fitted by plotting the logarithmic (log) σ versus log (P-P) and incrementally varying P until the best linear fit is obtained (Eq. (2)),

$$\sigma = A \cdot (P - P_c)^t \quad (\text{for } P > P_c) \tag{1}$$

$$\log \sigma = \log A + t \cdot \log(P - P_c) \tag{2}$$

where A is a scaling factor, P is the percolation threshold, σ is the conductivity of the CPCs, P is the FLG content, and t is the critical exponent, which depends on the geometry of the conducting network. The experimental data were well fitted ($R^2 = 0.9968$) according to Eq. (2). The percolation threshold P calculated using Eq. (2) was 2.7 wt%. It has been reported that composites near electrical percolation threshold generally show the highest sensitivity because of the just formed conductive networks are vulnerable to the external stimuli [12]. To obtain a stable electrical signal, the SGFs containing 3 wt%, 5 wt%, and 7 wt% FLG, beyond the percolation threshold, were selected for further investigation.

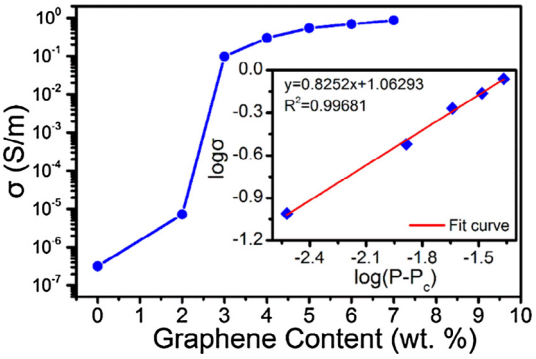

Fig. 2. Conductivity as a function of FLG content for SGFs; the insert shows a log-log plot of conductivity versus P-P above the percolation concentration P. (For interpretation of the references to colour in this figure legend, the reader is referred to the web version of this article.)

3.3. Elastic recovery behavior and mechanical hysteresis

Good mechanical reliability is indeed one of the most important properties of strain sensors for their practical applications. The representative strain-stress curves of SGFs with different FLG contents and their specific mechanical properties are shown in Fig. S4 (Supporting Information). The tensile strength of SBS/3G, SBS/5G and SBS/7G are 18.3 MPa, 13.3 MPa and 5.0 MPa, respectively. It is observed that the SGFs with higher FLG loading show lower tensile strength and the elongation at break reduces also due to increasing agglomeration and porosity acting as initiating site for fatal failure. However, the stretchability of the SGFs with elongation at breaks of >700% for SBS/3G and still over 200% for SBS/7G fulfill the requirements of the flexible strain sensors. Therefore, all the three SGFs can meet the strain sensing requirement due to their large elongation at breaks (the minimum is >200%).

The elastic recovery and mechanical hysteresis play a fundamental role in sensor reproducibility and reliability. For the elastic recovery tests, SGFs were first stretched to 50% and were then released to the original length at a strain rate of 20 mm min^{-1}. Fibers were subsequently stretched to 100%, 200%, 400%, and 600% (if they did not break) before releasing to the initial length. The representative elastic recovery behavior of the SBS/3G fiber is displayed in Fig. 3a. It was observed that the loading and unloading paths of curves were different for each cycle under the same strain, suggesting a mechanical hysteresis in these SGFs. The elastic recovery (ER) at each applied strain (ε) was calculated using Eq. (3) [31].

$$ER_{\varepsilon} = \frac{\varepsilon - \varepsilon_R}{\varepsilon} \times 100 \quad (3)$$

where ε is the applied strain and ε is the residual strain after stretching-releasing tests (Fig. 3a). For SGFs with different FLG loadings, the elastic recovery showed similar trends that initially increased with applied strain before eventually falling (Fig. 3b). For applied strain above 100%, it was found that the elastic recovery decreased gradually with increased FLG loading. This is because an irreversible slip is likely to happen between the graphene layers and between the graphene sheets and SBS chains under significant mechanical deformation, even when strong interfacial adhesion was observed. Although the FLG deteriorates the mechanical properties still the elastic properties of SBS (in all the SGFs) persisted with good elastic recovery properties.

The mechanical hysteresis of these SBS/3G fibers was further investigated by repetitive stretching and releasing for five cycles under the stepwise increase deformations of 50%, 100%, 200%, 400%, and 600% at a strain rate of 20 mm min^{-1} (Fig. 3c and 3d). At each applied strain (take 50% applied strain as an example), both the mechanical hysteresis, stress softening (defined as the reduction in stress by strain history, Fig. 3c), and Young's modulus decreased with increasing number of cycles. It is noted that most mechanical hysteresis and stress softening occurred in the first cycle. According to previous report, the mechanical hysteresis and stress softening for butadiene-styrene block copolymers are typically attributed to the breakage of styrene domains upon stretching [32,33]. In our case, the mechanical hysteresis and stress softening originate from the irreversible deformations during stretching due to slippage between graphene sheets, graphene sheets and SBS chains, and between polymer chains in the hard segment domains. During the first stretching run, instable contacts and inner bonds formed during the fiber preparation brake irreversibly and do not reform during relaxation. Thus the second deformation process and all the following need much less power to reach same elongations. These observations are in agreement with the previous reports on cyclic behavior of butadiene-styrene block copolymers [34] as well as polyurethane composites [25].

3.4. Electromechanical properties

3.4.1. Effect of FLG loading on the strain sensing behavior

The content of conductive fillers has a significant impact on the strain sensing behavior of a sensor [12]. The effect of FLG content on the strain sensing behavior of SGFs was well investigated. Fig. 4a shows the relative resistance change (ΔR/R, where ΔR = R − R, R represents the transient resistance during the testing process, and R is the initial resistance of the sample.) of the SGFs as a function of the applied strain at a strain rate of 5 mm min^{-1}. The sensitivity is defined as the ratio of the instantaneous change in resistance (ΔR) to the resistance (R) at the initial state. The SGFs with different FLG loading exhibited similar piezoresistive responses at the initial stages of deformation, whereby ΔR/R increased with applied strain, which can be attributed to the disconnection of FLG in SBS matrix and increased tunneling resistance, both resulting in an increase in resistance. Note that the slope coefficient of the ΔR/R-strain curve increases rapidly under larger applied strain, which becomes visible when plotting Fig. 4a in linear scale (see Fig. S5, Supporting Information). This is ascribed to a significant amount of interruption of the conductive graphene networks under tremendous applied strain, leading to a dramatic reduction of the conductive pathways.

The variation of composites' resistivity due to mechanical deformation can be quantified through determination of the Gauge factor (GF, defined as (ΔR/R)/ε), which is usually applied to evaluate the sensitivity of strain sensors [35]. The GF of SGFs with different FLG contents as a function of applied strain is shown in Fig. 4b. It is observed that a small change in FLG contents gives rise to an obvious change in the slope coefficient of the GF-strain curve when strain is above 20%, indicating that the sensor sensitivity is strongly dependent on the FLG content. The GF are found to be 1160, 54, and 28 for SBS/3G, SBS/5G, and SBS/7G composite fibers, respectively, under the strain of 50%. Obviously the composite fiber with lower FLG content shows higher sensitivity. For the composite fiber containing FLG contents slightly above the percolation threshold (i.e. 3 wt%), the amounts of FLG are just enough to form a sparse conductive network. As a result, the composite fibers with such sparse network structure show lower electrical conductivity and are more sensitive to deformation, reflected by higher GF values at the same strain level. On the contrary, for the composite fiber containing FLG contents much higher than the percolation threshold (like 7 wt%), the amounts of FLG are sufficient to form dense conductive network. During stretching, the destruction of conductive networks will not be as effective as that in the composite fiber with lower FLG loading because more contacts must be broken to

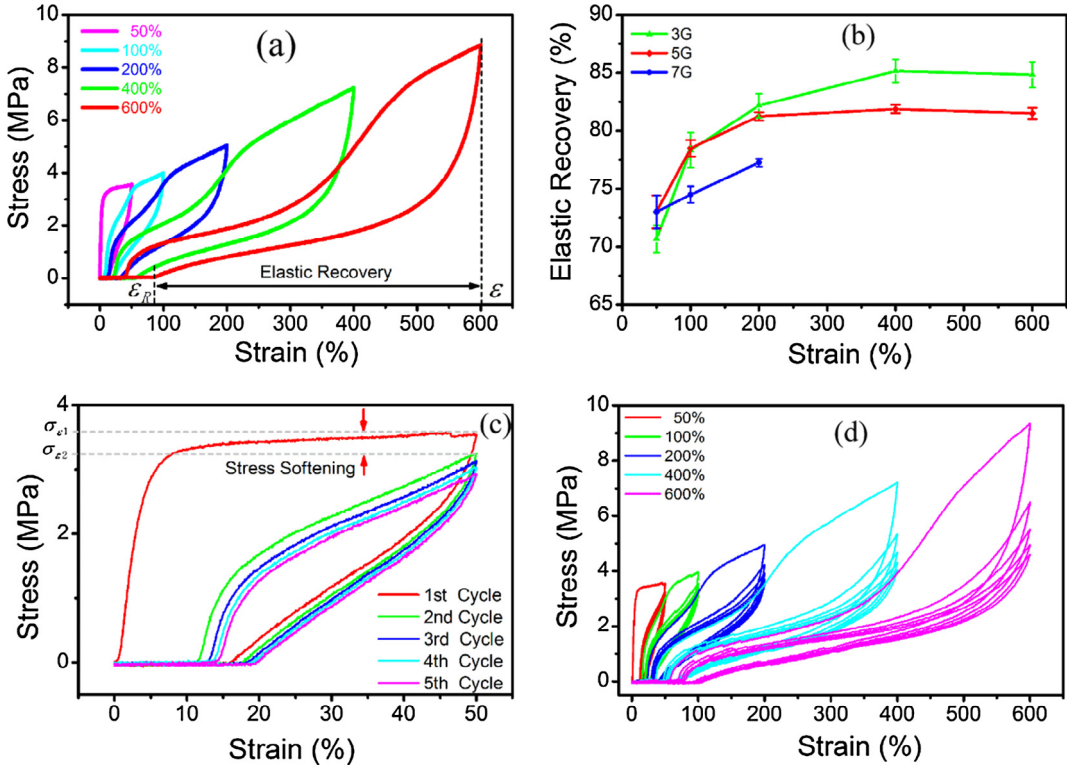

Fig. 3. (a) Stress-strain curves of SBS/3G fibers for cyclic elastic recovery tests with growing maximal strain from 50 to 600%, (b) Elastic recovery of SGFs during cyclic stretching-releasing tests as function of growing maximum strain, (c) Mechanical hysteresis of 50% strain for 5 cycles of SBS/3G fibers, (d) Mechanical hysteresis of SBS/3G fibers for 5 stretching-releasing cycles at each strain of 50%, 100%, 200%, 400%, and 600%. (For interpretation of the references to colour in this figure legend, the reader is referred to the web version of this article.)

reduce the number of conductive paths significantly. Therefore, the piezoresistive sensitivity of the composite fiber decrease with the increase of FLG contents at the same strain level.

According to the above discussion, the composite fibers with higher FLG contents show higher electrical conductivity and are more robust to resist deformation. Thus the maximum workable strain range should increase with increasing FLG contents. In this work, the maximum workable strain range for SBS/3G, SBS/5G, and SBS/7G were 118%, 230%, and 70%, respectively, since at these strains the resistance reaches the limit to be measurable with our instrumentation. This limitation results in a paradoxically lower maximum workable strain range of SBS/7G composite fiber compared to that of SBS/5G composite fiber. As mentioned above, the SBS/7G composite fiber shows lowest tensile strength and the lowest elongation at break (230%) because of the large FLG agglomerates and the high porosity formed inside the fiber. The conductive network in this SGF containing theses larger agglomerated and porous FLG structures can be easier and irreversibly destroyed when stretching the SBS/7G composite fiber above 73% strain, which causes a dramatically increase in resistance, and when the strain reaches ca. 82%, the limit of the measuring range of our apparatus is reached (see Fig. S6, Supporting Information). As a result, the SBS/7G composite fiber shows lower workable strain range. This shows that the content of filler can be fitted to the desired strain range.

The comparison of the sensing performance of the SGFs sensor with that of recently reported flexible strain sensors is shown in Fig. 4c. It is observed that the sensing performance of SGFs is very competitive to these recently reported strain sensors [1,5,7,20,36–44].

For practical applications, dynamic durability is also desirable for wearable strain sensors since very large, complex, and dynamic strains should be accommodated by these sensors [2]. Therefore, to investigate the dynamic durability and reliability of these SGFs, the dynamic strain sensing behavior was studied with a cyclic stretching-releasing profile between 0% and 50% strain (as shown in Fig. 5a). For all samples, it was observed that the $\Delta R/R$ increased with increasing strain and decreased with decreasing strain in each cycle. Nevertheless, in the first cycle, after releasing, a higher $\Delta R/R$ value than the initial one was observed, suggesting the conductive graphene networks could not be fully recovered to initial state known as electromechanical hysteresis. This is mainly caused by the mechanical hysteresis of SBS matrix mentioned above as well as the interaction between graphene and SBS. The electromechanical hysteresis becomes inapparent in the following cycles, which means most electromechanical hysteresis occurred in the first cycle. This is in accordance with the mechanical hysteresis of SGFs. It is worth noting that the "shoulder peaks" reported in previous literature [12,14] were not observed in SGFs, illustrating the good stability of the conductive graphene networks of SGFs.

In order to perform a more quantificational estimation of sensitivity and dynamic durability, the ratios between the reduction of peak value during cyclic strains (D) and $\Delta R/R$ peak of the first cycle (P) for SGFs (Fig. 5b shows the representation of D and P determination) are shown in Fig. 5c. The ratio of D/P represents the recovery ratio of conductive networks under cyclic strain. The increase of D/P was also considered as a reduction of sensitivity during cyclic strains [12]. The ratios were 20.4%, 7.9% and 3.4% for SBS/3G, SBS/5G, and SBS/7G, respectively. It is evident that the SGFs with lower loading of FLG show higher D/P ratio. This indicates that the SGFs with higher FLG content have more stable conductive networks due to the much denser graphene network structure as compared to those with lower content. The average amplitude (A, see Fig. 5b) of these SGFs is also shown in Fig. 5c, where much higher amplitude values are observed for samples with lower FLG loadings, indicating higher sensitivity. These results agree well with

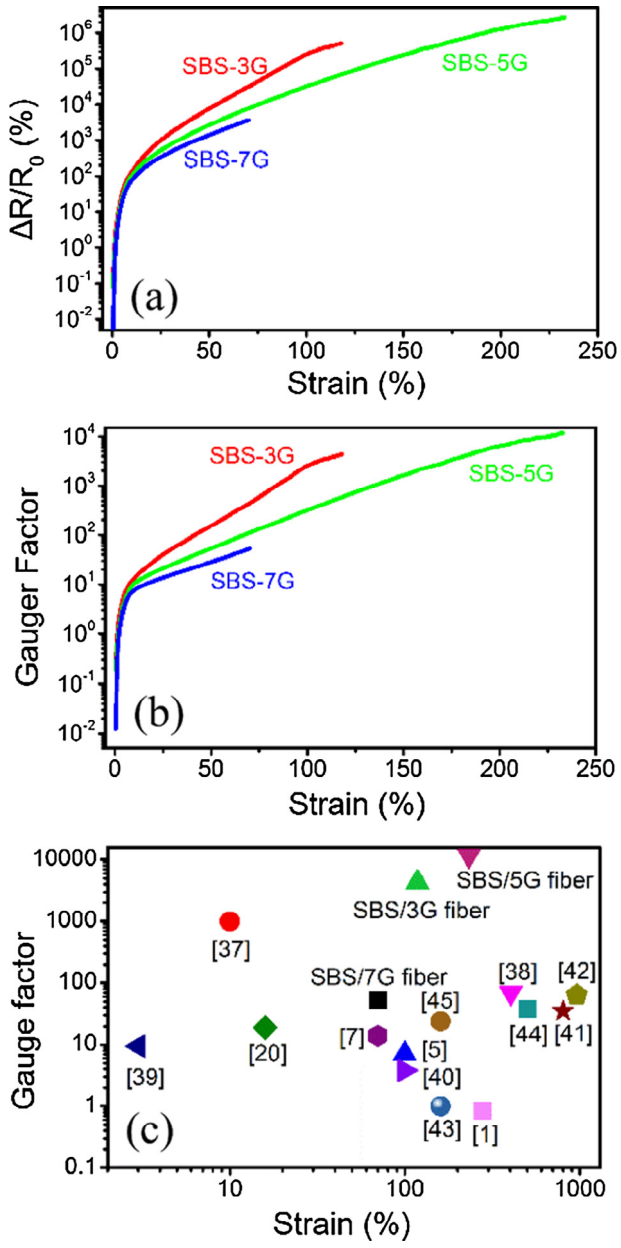

Fig. 4. (a) ΔR/R and (b) GF as a function of applied strain, respectively. (Note: Gauge factor axis are in Log, see Fig. S5 for actual experimental values) (c) Comparison of the performance of the SGFs sensor with that of recently reported flexible strain sensors. (For interpretation of the references to colour in this figure legend, the reader is referred to the web version of this article.)

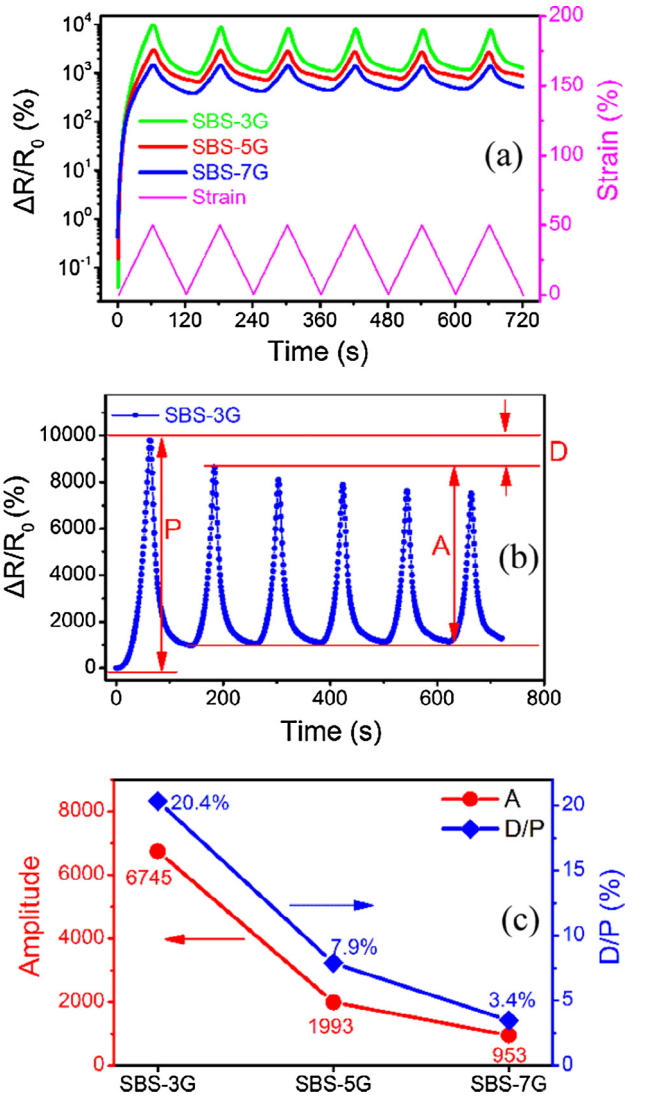

Fig. 5. (a) The dynamic strain sensing behavior of SGFs fiber with different FLG loading under cyclic stretching and releasing at a strain between 0 and 50%, (b) The representation of the determination of the recovery ratio (D/P) and amplitude A, (c) The recovery ratio D/P of conductive network and amplitude A of ΔR/R peak during dynamic stretching in dependence of FLG content. (For interpretation of the references to colour in this figure legend, the reader is referred to the web version of this article.)

those in Fig. 4. Compared with previous studies [45], there is no obvious downward drifting of the amplitude, reconfirming the excellent stability of the conductive networks during cyclic loading-unloading. Accordingly, SGFs with the combination of large workable strain range, high sensitivity, and good reliability can be qualified for practical applications in wearable strain sensor. SBS/3G fiber was used for further investigations because of its higher sensitivity.

3.4.2. Effect of applied strain and strain rate on the strain sensing behavior

To investigate the reliability and stability of SGFs at different applied strains, the dynamic strain sensing behavior was performed with a cyclic loading-unloading of 5%, 10%, 25%, 50% and 100% strain (as shown in Fig. 6a). For all applied strain levels, the SGFs based strain sensor shows good reversibility and reproducibility starting from the second cycle. In previous studies [46,47], the stable responsive curve was reached only after several extension cycles due to the unstable conductive networks. By contrast, the conductive network of SGFs is more stable and robust during the dynamic loading-unloading process. This could be attributed to both the homogeneous dispersion of FLG within SBS matrix and the denser graphene networks.

In practical application, dynamic reliability under different frequency is also essential for wearable strain sensors [2]. Thus, the dynamic strain sensing behavior was performed with a cyclic stretching-releasing at different strain rates of 5, 20 and 500 mm min^{-1} (corresponding to 50, 200 and 500% min^{-1}) to a maximum applied strain of 50%. As shown in Fig. 6b, the ΔR/R of the SGFs based strain sensor exhibited almost no rate dependence within the tested strain rate range (5–50 mm min^{-1}) to the applied strain. The reduction of ΔR/R peaks at 50 mm min^{-1} is due to the multi-

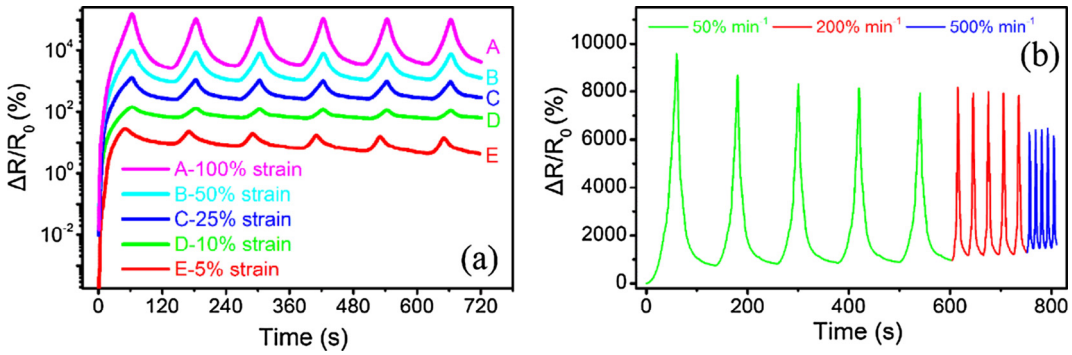

Fig. 6. (a) The dynamic strain sensing behavior of SBS/3G fiber with a cyclic loading-unloading of 5%, 10%, 25%, 50% and 100%, (b) strain sensing behavior of SBS/3G fiber with a cyclic stretching-releasing at different strain rate. (For interpretation of the references to colour in this figure legend, the reader is referred to the web version of this article.)

meter which could not keep pace with the resistance variation of SGFs based strain sensor.

3.5. Modeling and mechanism

As reported in previous literature, the dominant piezoresistive mechanism of the FLG-polymer nanocomposites based strain sensors was ascribed to be built on the tunneling effect [48,49]. Herein, a model based on tunneling theory is carried out to explore the above strain sensing behavior of SGFs. According to the model [50] derived from tunneling theory by Simmons [51], the total resistance R of the composites can be calculated using Eqs. (4) and (5):

$$R = \left(\frac{L}{N}\right)\left(\frac{8\pi hs}{3\gamma a^2 e^2}\right)\exp(\gamma s) \tag{4}$$

$$\gamma = \frac{4\pi\sqrt{2m\varphi}}{h} \tag{5}$$

where L is the number of particles forming a single conducting path, N is the number of conductive paths, h is the Plank's constant, s is the smallest distance between conductive particles, a^2 is the effective cross-section, e is the electron charge, m the electron mass, and φ the height of potential barrier between adjacent particles.

During external stress application onto the SGFs, the resistance will change owing to particle separation and the increase of interparticle distance. Assuming that the FLG sheet separation proportionally varies from s (the initial particle separation) to s under the applied strain, and the number of conductive paths decreases from N to N. Then, it can be expressed as follows Eq. (6):

$$s = s_0(1 + b\varepsilon) \tag{6}$$

where b is a constant. In consideration of the high rate of resistivity increase at larger strain, it is assumed that the number of conductive pathways changes at a much higher rate, and can be expressed as follows Eq. (7) [52].

$$N = \frac{N_0}{\exp(A\varepsilon + B\varepsilon^2 + C\varepsilon^3 + D\varepsilon^4)} \tag{7}$$

where A, B, C, and D are constants.

The substitution of Eqs. (56) and (7) into (4) yields

$$\frac{\Delta R}{R_0} = \frac{R - R_0}{R_0} = \left(\frac{Ns}{N_0 s_0}\right)\exp[\gamma(s - s_0)] - 1 = (1 + b\varepsilon)\exp\left[(A + \gamma b s_0)\varepsilon + B\varepsilon^2 + C\varepsilon^3 + D\varepsilon^4\right] - 1 \tag{8}$$

As can be seen from Fig. 7, the model derived from tunneling theory matches the experimental data of SGFs quite well (R^2 = 0.9997).

To better understand the strain sensing behavior of the SGFs strain sensors, the evolutions of conductive graphene networks during stretching and releasing are schematically represented in Fig. 8 based on above results and discussion. Fig. 9 shows the plot of ΔR/R and stress as a function of applied strain in a cyclic stretching-releasing process for the first two cycles. Each zone is marked by a number in the figure. According to tunneling effect, within a critical distance between neighboring FLG sheets, electrons can path through thin polymer layers and form quantum tunneling junctions. The tunneling resistance between two adjacent few layer graphene sheets can be approximately estimated by Simmons's theory for tunneling resistance:

$$R_{tunnel} = \frac{h^2 d}{Ae^2\sqrt{2m\lambda}}\exp\left(\frac{4\pi d}{h}\sqrt{2m\lambda}\right) \tag{9}$$

where A is the cross sectional area of the tunneling junction, h is Plank's constant, d is the distance between adjacent FLG sheets, e is the single electron charge, m is the mass of the electron, and λ is the height of energy barrier for polymers. The tunneling critical distance between two parallel FLG sheets insulated with polymers was determined to be around 2–3 nm. Thus, the changes in the tunneling gaps play crucial roles in the piezoresistive response. In the original state, the SGFs show relatively compact graphene networks and minimum tunneling distance. As a result, the SGFs showed a minimum resistance. When the SGFs are stretched (Fig. 9, zone 1), the flexible FLG sheets wriggled with the SBS chains, leading an increase in the tunneling distance between FLG sheets (Fig. 8b,[1] green dotted ellipse). The increase in tunneling distance results in an increase in R and destruction of the conductive pathway. Simultaneously, some new conductive pathways are formed due to the reduction of tunneling distance (Fig. 8, green solid ellipse). The destruction and reconstruction of the conductive pathways coexist in the whole process. However, the destruction of the conductive graphene networks is predominant in the stretching process, so an increase of ΔR/R is observed. During the hold period at strained state (Fig. 9, zone 2), both the stress and ΔR/R decreased over time, suggesting the partial reconstruction of conductive networks owing to the creep in the SBS matrix. During the releasing process (Fig. 9, zone 3), the reconstruction of the conductive graphene networks is predominant (Fig. 8c, green dotted ellipse), resulting in a sharp drop in ΔR/R. When the fiber is held at zero strain for 2 min (Fig. 9, zone 4), the ΔR/R continues to decrease due to the further reduction of tunneling distance. It should be noted that the ΔR/R at the end of the first cycle was observed to be higher than that of the unstretched SGF. This is because of the irreversible destruction of conductive

[1] For interpretation of color in Fig. 8, the reader is referred to the web version of this article.

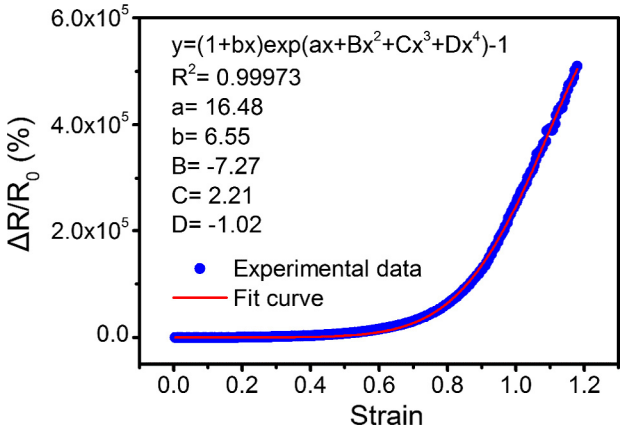

Fig. 7. Experimental ΔR/R as a function of applied strain for SBS/3G fiber and the fitted curve. (For interpretation of the references to colour in this figure legend, the reader is referred to the web version of this article.)

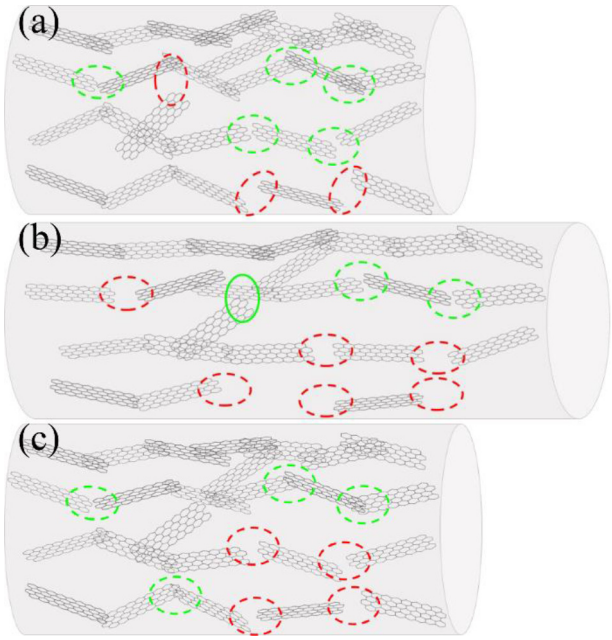

Fig. 8. Schematic illustration for the evolution of the conductive network in a stretching-releasing process. (a) The initial state; (b) the stretched state; (c) the relaxed state. (For interpretation of the references to colour in this figure legend, the reader is referred to the web version of this article.)

pathways (Fig. 8c, red dotted ellipse). When the fiber is re-stretched in the second cycle (Fig. 9, zone 6), at first both the stress and ΔR/R did not increase with applied strain until it reached to 15%. This is also caused by hysteresis. In the following process, similar phenomenon occurs in zone 6, 7, and 8 as in zone 2, 3, and 4, respectively. Notably, the ΔR/R at the end of the first cycle and second cycle are nearly the same, demonstrating that the conductive graphene networks can reach the stable state after only one cycle.

4. Conclusions

SGFs were fabricated through a facile and scalable wet spinning process and evaluated as piezoresistive strain sensors. It was demonstrated that the FLG content has a significant impact on the strain sensing behavior of these SGFs. The SGFs near the electrical percolation threshold show the highest sensitivity with

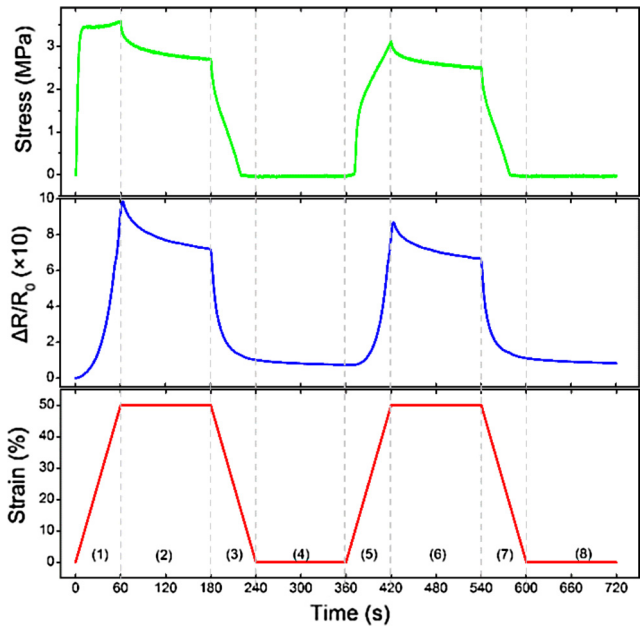

Fig. 9. Stress and ΔR/R change by applied strain for SBS/3G fiber in a cyclic stretching-releasing test under application of 50% strain for the first two cycles. Numbers show the stretching, releasing, and relaxation zones. (For interpretation of the references to colour in this figure legend, the reader is referred to the web version of this article.)

applied strain. The cyclic stretching-releasing test results indicate that the SGFs with higher FLG content show better stability and reliability but lower amplitude. This is attributed to the more robust conductive network consisting of dense few layer graphene sheets, which is harder to interrupt. Furthermore, the electromechanical hysteresis occurring in the first cycle is mainly caused by irreversible disconnection of conductive paths caused by slippage between graphene sheets and between graphene and SBS chains as well as between polymer chains in the hard segment domains. Overall, SBS/5G fiber revealed the widest workable strain range of nearly 250% and highest sensitivity at large strains. Otherwise, the composite fibers with the lowest usable FLG content, SBS/3G, combines the higher sensitivity at lower stains (GF of 160 at a strain of 50% and that of 2546 at a strain of 100%) and a still high workable strain range of >110%. All composite fibers exhibit appropriate stability in sensing after first stretching-releasing run. As proved by both the experimental observations and theoretical analysis, the strong graphene-SBS interfacial interactions and the stable conductive networks of SGFs contribute to the superior properties of the strain sensors. An analytical model derived from tunneling theory was used to investigate the strain sensing behavior of SGFs. Results showed that the model matched with the experimental data of SBS/FLG fibers quite well and the change in tunneling distance owing to stretching was responsible for the strain sensing behaviors. Therefore, the reported methodology, material selection, and design can be used to re-fabricate various piezoresistive strain sensors based on other related polymers, carbon-based materials and 2D-materials with high performance.

Acknowledgements

This work was supported by Shanghai Fundamental Research Projects (Project No. 16JC1400701), Program for Changjiang Scholars and Innovative Research Team in University (IRT16R13), Innovation Program of Shanghai Municipal Education Commission (E00055), and Opening Project of State Key Laboratory of for Mod-

ification of Chemical Fibers and Polymer Materials, Donghua University (Contract Number: LK1607).

Appendix A. Supplementary material

Supplementary data associated with this article can be found, in the online version, at https://doi.org/10.1016/j.compositesa.2017.11.027.

References

[1] Yamada T, Hayamizu Y, Yamamoto Y, Yomogida Y, Izadi-Najafabadi A, Futaba DN, et al. A stretchable carbon nanotube strain sensor for human-motion detection. Nat Nanotechnol 2011;6(5):296–301.
[2] Amjadi M, Kyung K-U, Park I, Sitti M. Stretchable, skin-mountable, and wearable strain sensors and their potential applications: a review. Adv Funct Mater 2016;26(11):1678–98.
[3] Wang Y, Wang L, Yang TT, Li X, Zang XB, Zhu M, et al. Wearable and highly sensitive graphene strain sensors for human motion monitoring. Adv Funct Mater 2014;24(29):4666–70.
[4] Lipomi DJ, Vosgueritchian M, Tee BCK, Hellstrom SL, Lee JA, Fox CH, et al. Skin-like pressure and strain sensors based on transparent elastic films of carbon nanotubes. Nat Nano 2011;6(12):788–92.
[5] Yan C, Wang J, Kang W, Cui M, Wang X, Foo CY, et al. Highly stretchable piezoresistive graphene-nanocellulose nanopaper for strain sensors. Adv Mater 2014;26(13):2022–7.
[6] Park S-J, Kim J, Chu M, Khine M. Highly flexible wrinkled carbon nanotube thin film strain sensor to monitor human movement. Adv Mater Technol 2016;1(5).
[7] Amjadi M, Pichitpajongkit A, Lee S, Ryu S, Park I. Highly stretchable and sensitive strain sensor based on silver nanowire-elastomer nanocomposite. ACS Nano 2014;8(5):5154–63.
[8] Natarajan TS, Eshwaran SB, Stöckelhuber KW, Wießner S, Pötschke P, Heinrich G, et al. Strong strain sensing performance of natural rubber nanocomposites. ACS Appl Mater Interfaces 2017;9(5):4860–72.
[9] Georgousis G, Pandis C, Chatzimanolis-Moustakas C, Kyritsis A, Kontou E, Pissis P, et al. Study of the reinforcing mechanism and strain sensing in a carbon black filled elastomer. Composites Part B 2015;80:20–6.
[10] Zhao JH, Dai K, Liu CG, Zheng GQ, Wang B, Liu CT, et al. A comparison between strain sensing behaviors of carbon black/polypropylene and carbon nanotubes/polypropylene electrically conductive composites. Composites Part A 2013;48:129–36.
[11] Ke K, Pötschke P, Wiegand N, Krause B, Voit B. Tuning the network structure in poly(vinylidene fluoride)/carbon nanotube nanocomposites using carbon black: toward improvements of conductivity and piezoresistive sensitivity. ACS Appl Mater Interfaces 2016;8(22):14190–9.
[12] Duan L, Fu S, Deng H, Zhang Q, Wang K, Chen F, et al. The resistivity-strain behavior of conductive polymer composites: stability and sensitivity. J Mater Chem A 2014;2(40):17085–98.
[13] Vertuccio L, Vittoria V, Guadagno L, De Santis F. Strain and damage monitoring in carbon-nanotube-based composite under cyclic strain. Composites Part A 2015;71:9–16.
[14] Liu H, Li Y, Dai K, Zheng G, Liu C, Shen C, et al. Electrically conductive thermoplastic elastomer nanocomposites at ultralow graphene loading levels for strain sensor applications. J Mater Chem C 2016;4(1):157–66.
[15] Liu Y, Zhang D, Wang K, Liu Y, Shang Y. A novel strain sensor based on graphene composite films with layered structure. Composites Part A 2016;80:95–103.
[16] Lee S, Shin S, Lee S, Seo J, Lee J, Son S, et al. Ag nanowire reinforced highly stretchable conductive fibers for wearable electronics. Adv Funct Mater 2015;25(21):3114–21.
[17] Lee C, Wei X, Kysar JW, Hone J. Measurement of the elastic properties and intrinsic strength of monolayer graphene. Science 2008;321(5887):385–8.
[18] Bae SH, Lee Y, Sharma BK, Lee HJ, Kim JH, Ahn JH. Graphene-based transparent strain sensor. Carbon 2013;51:236–42.
[19] Costa P, Ribeiro S, Lanceros-Mendez S. Mechanical vs. electrical hysteresis of carbon nanotube/styrene–butadiene–styrene composites and their influence in the electromechanical response. Compos Sci Technol 2015;109:1–5.
[20] Park M, Im J, Shin M, Min Y, Park J, Cho H, et al. Highly stretchable electric circuits from a composite material of silver nanoparticles and elastomeric fibres. Nat Nanotechnol 2012;7(12):803–9.
[21] Costa P, Silvia C, Viana JC, Lanceros Mendez S. Extruded thermoplastic elastomers styrene–butadiene–styrene/carbon nanotubes composites for strain sensor applications. Composites Part B 2014;57:242–9.
[22] Liu YT, Xie XM, Ye XY. High-concentration organic solutions of poly(styrene-co-butadiene-co-styrene)-modified graphene sheets exfoliated from graphite. Carbon 2011;49(11):3529–37.
[23] Chen S, Ma W, Cheng Y, Weng Z, Sun B, Zhu M, et al. Scalable non-liquid-crystal spinning of locally aligned graphene fibers for high-performance wearable supercapacitors. Nano Energy 2015;15:642–53.
[24] Ma W, Chen S, Yang S, Chen W, Weng W, Zhu M, et al. Bottom-up fabrication of activated carbon fiber for all-solid-state supercapacitor with excellent electrochemical performance. ACS Appl Mater Interfaces 2016;8(23):14622–7.
[25] Seyedin MZ, Razal JM, Innis PC, Wallace GG. Strain-responsive polyurethane/PEDOT: PSS elastomeric composite fibers with high electrical conductivity. Adv Funct Mater 2014;24(20):2957–66.
[26] Zhang X, Feng Y, Tang S, Feng W. Preparation of a graphene oxide–phthalocyanine hybrid through strong π–π interactions. Carbon 2010;48(1):211–6.
[27] Shen B, Zhai W, Chen C, Lu D, Wang J, Zheng W. Melt blending in situ enhances the interaction between polystyrene and graphene through π–π stacking. ACS Appl Mater Interfaces 2011;3(8):3103–9.
[28] Ramanathan T, Abdala AA, Stankovich S, Dikin DA, Herrera Alonso M, Piner RD, et al. Functionalized graphene sheets for polymer nanocomposites. Nat Nano 2008;3(6):327–31.
[29] Li H, Wu S, Wu J, Huang G. Enhanced electrical conductivity and mechanical property of SBS/graphene nanocomposite. J Polym Res 2014;21(5):456.
[30] Villmow T, Pegel S, Pötschke P, Heinrich G. Polymer/carbon nanotube composites for liquid sensing: model for electrical response characteristics. Polymer 2011;52(10):2276–85.
[31] Seyedin MZ, Razal JM, Innis PC, Jalili R, Wallace GG. Achieving outstanding mechanical performance in reinforced elastomeric composite fibers using large sheets of graphene oxide. Adv Funct Mater 2015;25(1):94–104.
[32] Leblanc JL. Stress–strain behavior, hardness, and thermomechanical properties of butadiene–styrene block copolymers as a function of processing technique. J Appl Polym Sci 1977;21(9):2419–37.
[33] Niinomi M, Akovali G, Shen M. Polyblends of poly(styrene-b-butadiene-b-styrene) and polystyrene. II. Electron microscopy. J Macromol Sci B 1977;13(1):133–50.
[34] Costa P, Ferreira A, Sencadas V, Viana JC, Lanceros-Méndez S. Electro-mechanical properties of triblock copolymer styrene–butadiene–styrene/carbon nanotube composites for large deformation sensor applications. Sensor Actuat A 2013;201:458–67.
[35] Granero AJ, Wagner P, Wagner K, Razal JM, Wallace GG, Panhuis MIH. Highly stretchable conducting SIBS-P3HT fibers. Adv Funct Mater 2011;21(5):955–62.
[36] Li X, Zhang RJ, Yu WJ, Wang KL, Wei JQ, Wu DH, et al. Stretchable and highly sensitive graphene-on-polymer strain sensors. Sci Rep-Uk. 2012;2.
[37] Slobodian P, Riha P, Saha P. A highly-deformable composite composed of an entangled network of electrically-conductive carbon-nanotubes embedded in elastic polyurethane. Carbon 2012;50(10):3446–53.
[38] Tian H, Shu Y, Cui Y-L, Mi W-T, Yang Y, Xie D, et al. Scalable fabrication of high-performance and flexible graphene strain sensors. Nanoscale 2014;6(2):699–705.
[39] Muth JT, Vogt DM, Truby RL, Mengüç Y, Kolesky DB, Wood RJ, et al. Embedded 3D printing of strain sensors within highly stretchable elastomers. Adv Mater 2014;26(36):6307–12.
[40] Boland CS, Khan U, Backes C, O'Neill A, McCauley J, Duane S, et al. Sensitive, high-strain, high-rate bodily motion sensors based on graphene-rubber composites. ACS Nano 2014;8(9):8819–30.
[41] Ryu S, Lee P, Chou JB, Xu R, Zhao R, Hart AJ, et al. Extremely elastic wearable carbon nanotube fiber strain sensor for monitoring of human motion. ACS Nano 2015;9(6):5929–36.
[42] Seyedin S, Razal JM, Innis PC, Jeiranikhameneh A, Beirne S, Wallace GG. Knitted strain sensor textiles of highly conductive all-polymeric fibers. ACS Appl Mater Interfaces 2015;7(38):21150–8.
[43] Wang C, Li X, Gao E, Jian M, Xia K, Wang Q, et al. Carbonized silk fabric for ultrastretchable, highly sensitive, and wearable strain sensors. Adv Mater 2016;28(31):6640–8.
[44] Cho D, Park J, Kim J, Kim T, Kim J, Park I, et al. Three-dimensionally continuous conductive nanostructure for highly sensitive and stretchable strain sensor. ACS Appl Mater Interfaces 2017;9(20):17369–78.
[45] Lin L, Liu S, Zhang Q, Li X, Ji M, Deng H, et al. Towards tunable sensitivity of electrical property to strain for conductive polymer composites based on thermoplastic elastomer. ACS Appl Mater Interfaces 2013;5(12):5815–24.
[46] Lin Y, Liu S, Chen S, Wei Y, Dong X, Liu L. A highly stretchable and sensitive strain sensor based on graphene-elastomer composites with a novel double-interconnected network. J Mater Chem C 2016;4(26):6345–52.
[47] Liu H, Gao J, Huang W, Dai K, Zheng G, Liu C, et al. Electrically conductive strain sensing polyurethane nanocomposites with synergistic carbon nanotubes and graphene bifillers. Nanoscale 2016;8(26):12977–89.
[48] Lee C, Jug L, Meng E. High strain biocompatible polydimethylsiloxane-based conductive graphene and multiwalled carbon nanotube nanocomposite strain sensors. Appl Phys Lett 2013;102(18).
[49] Zhao J, He CL, Yang R, Shi ZW, Cheng M, Yang W, et al. Ultra-sensitive strain sensors based on piezoresistive nanographene films. Appl Phys Lett 2012;101(6).
[50] Zhang X-W, Pan Y, Zheng Q, Yi X-S. Time dependence of piezoresistance for the conductor-filled polymer composites. J Polym Sci Pol Phys 2000;38(21):2739–49.
[51] Simmons JG. Generalized formula for the electric tunnel effect between similar electrodes separated by a thin insulating film. J Appl Phys 1963;34(6):1793–803.
[52] Sheng P, Sichel EK, Gittleman JI. Fluctuation-induced tunneling conduction in carbon-polyvinylchloride composites. Phys Rev Lett 1978;40(18):1197–200.